Astron. Astrophys. 332, 479–492 (1998)

ASTRONOMY AND ASTROPHYSICS

PKS 1932-464: a jet-cloud interaction in a radio galaxy?⋆

M. Villar-Martín[1], C. Tadhunter[1], R. Morganti[2,3], N. Clark[4], N. Killeen[3], and D. Axon[4]

[1] Department of Physics, University of Sheffield, Sheffield S3 7RH, UK
[2] Istituto di Radioastronomia, Via Gobetti 101, I-40129 Bologna, Italy
[3] CSIRO-ATNF, PO Box 76, Epping NSW 2121, Australia
[4] Space Telescope Science Institute, 3700 San Martin Drive, Baltimore MD21218, USA

Received 12 November 1997 / Accepted 22 December 1997

Abstract. We present optical and radio images, and long-slit spectra of the radio galaxy PKS 1932-464 (z=0.230). Our main goal is to determine whether the observed properties of the extended emission line nebulosity in this object show evidence for interactions between the radio jet and the extended ionized gas, or whether they can be explained in terms of the illumination of the extended gas by the active nucleus. Although the data do not show compelling evidence for jet-cloud interactions, the existence of two well distinguished emitting line regions with very different kinematics and ionization levels suggests the presence of such interactions. The large-scale gas distribution is complex and suggests a gravitational interaction between the host galaxy of PKS 1932-464 and a nearby companion galaxy. The detection of a broad Hα emission line in the nuclear spectrum of the object provides evidence that this object is a broad line radio galaxy (BLRG) rather than a narrow line radio galaxy (NLRG) as previously supposed.

Key words: galaxies: individual: PKS 1932-464 – galaxies: ISM – galaxies: jets – galaxies: active – radio continuum: galaxies

1. Introduction

The general properties of the extended gas of most powerful radio galaxies at low redshift can be explained in terms of the illumination of the ambient gas by the active nucleus. However, there are some low and intermediate redshift radio galaxies (z$<$0.5) in which both the kinematics and the morphology of the extended emission line regions (EELR) provide strong evidence for powerful interactions between the radio jet and the extended gas (Clark 1996, Clark et al. 1996,1997a,b). This is particularly evident in high redshift (z $>$1) radio galaxies, which present collimated structures closely aligned with the radio axis (Chambers et al. 1987, McCarthy et al. 1987) and highly perturbed kinematics (e.g. Mc.Carthy et al. 1996, van Ojik et al. 1996, Pentericci et al. 1997).

We are carrying out a spectroscopic study of a small sample of powerful radio galaxies at intermediate and low redshift to understand the processes associated with the interactions between the radio jets and the ambient gas, and to gauge the importance of shocks in determining the observed properties of these objects. The ultimate goal is to determine the relative importance of the jet-cloud interaction phenomenon in the general population of powerful radio galaxies.

In the first stage of this work we have carried out detailed spectroscopic and imaging observations of objects which were known from previous studies to be strong candidates for jet-cloud interactions (Clark 1996, Clark et al. 1996,1997a,b). The results provided compelling evidence for the strong influence that the shocks can have on the kinematics, morphology and physical properties of the gas.

As a continuation of this project, we have selected the radio source PKS 1932-464 (z=0.230) (J2000 RA: 19 35 56.6 δ: -46 20 41.8), which has an early-type host galaxy. Initially, this object was observed as part of the Tadhunter et al. (1993) spectroscopic survey of southern radio galaxies with radio flux $S_{2.7GHz} > 2$Jy. These early spectroscopic observations revealed an extensive emission line nebulosity extending out to a radius of 23 arcsec ($\sim$113 kpc[1]) along the radio axis. This marked PKS 1932-464 as an interesting object for future study, although the a priori case for a jet-cloud interaction in this object was not as strong as the objects discussed in Clark et al. (1996, 1997), we were simply aware that the emission lines are extended along the radio axis. We present below new optical spectroscopic, and optical and radio imaging observations which we use to disentangle which properties of the object are a consequence of AGN illumination, and which are due to jet-cloud interactions.

Send offprint requests to: M. Villar-Martin, Department of Physics, University of Sheffield, Sheffield S3 7RH, UK

⋆ Based on observations collected at Anglo Australian Observatory, Australia

[1] H_0 = 50 km s^{-1} Mpc^{-1} and q_0 = 0.0 assumed throughout.

2. Observations

2.1. Optical imaging

The optical images were obtained using the ESO Faint Object Spectrograph and Camera EFOSC 1 on the 3.6m telescope at La Silla Observatory, Chile, on the night of 12/7/94. The detector is a Tek CCD with 512×512 pixels^2 of 27 μm^2 giving an image field size of 5.2' × 5.2'. The projected pixel size is 0.61 arcsec. The observations were carried out in moderate seeing conditions (1.8 arcsec FWHM).

Images with two different filters were obtained. Filter #626 was used to obtain the [OII]+continuum images (λ_0=4586 Å $\Delta\lambda$=109 Å), while the continuum images were taken with filter #718 (λ_0=5445 Å $\Delta\lambda$=175 Å). Two 300 second exposures were obtained with the pure continuum filter and two 600 second exposures with the line+continuum filter. These two frames were combined afterwards to increase the signal-to-noise ratio.

To improve the resolution and reveal faint structures, the images were deconvolved using Lucy-Richardson's algorithm in the STSDAS package in IRAF. A star in the same frame was used as a PSF and the number of iterations needed to obtain similar spatial resolution in both the [OII]+continuum (10 iterations) and the pure continuum image (14 iterations). Once the LR algorithm was applied, the effective seeing (FWHM) after restoration is 1.1 arcsec.

2.2. Radio observations

PKS 1932−464 was observed with the Australia Telescope Compact Array (ATCA) on 1994 September 4, using a 6-km array configuration and the standard continuum correlator setup providing a bandwidth of 128 MHz with 16 independent 8-MHz channels. The ATCA allows observations at two simultaneous frequencies (1.3/2.3 GHz or 5/8 GHz) and to switch very rapidly between the two set of frequencies during the observations. We took advantage of this facility and we observed PKS 1932–464 in all four different frequencies (i.e. 1.3, 2.3, 5.8 and 8.6 GHz). At each frequency the source was observed for 6h in total, spread out in equal length cuts over 12h. Observing at 8.6 GHz enabled us to achieve a resolution of ∼1 arcsec, the highest resolution currently possible with ATCA.

The primary flux density calibrator (1934−638) was observed at the beginning and the secondary calibrator (1933–400) was observed every 30 min to track the complex antenna gains with time. The data were analyzed with the MIRIAD package (Sault, Teuben & Wright 1995). All images were produced with standard synthesis imaging, deconvolution and self-calibration methods. Additionally, all our images were made with uniform weighting, which provides a better synthesised beam (narrower main peak and smaller sidelobes) at the expense of the loss of some sensitivity.

Together with the total intensity I, images of the Stokes parameters Q and U were also produced and from these we obtained the polarized intensity image ($P = (Q^2 + U^2)^{1/2}$) and position-angle image ($\chi = 0.5 \arctan(U/Q)$). The rms noise of the signal-free portion of the I and P images are given in Table 1. The polarized intensity, and, as a consequence, the fractional polarization ($m = P/I$) were estimated only for the pixels for which $P > 5\sigma_{QU}$.

Table 1. Radio parameters

Freq.	Beam size arcsec (degrees)	σ_I mJy beam^{-1}	σ_P mJy beam^{-1}
1.3GHz	9.9x3.9 (p.a. 15)	4.0	1.0
2.3GHz	5.9x2.4 (p.a. 16)	1.4	0.6
5.8GHz	3.0x1.2 (p.a. 19)	1.5	0.2
8.6GHz	2.0x0.8 (p.a. 19)	1.4	0.3

Because all the observations were made with the same configuration, the beam size is different for each frequency. This makes it difficult to use the four frequencies for a study of spectral index, depolarization and rotation measure (RM). The beam sizes at different frequencies are given in Table 1.

2.3. Long-slit spectroscopy

The spectroscopic observations were carried out on the nights 27-28/9/94 using the Royal Greenwich Observatory (RGO) spectrograph on the Anglo Australian Telescope. The detector is a Tek CCD with 226×1024 pixels of 27 μm^2, resulting in a spatial scale of 0.81 arcsec per pixel. The 1.5 arcsec slit was oriented at PA 270.

We used two gratings with different spectral resolutions and at different angles to select a wide spectral range. The spectral dispersions obtained were 1.57 Å pixel^{-1} with the 600R grating and 0.80 Å pixel^{-1} with the 1200V grating.

The reduction of the data was done using standard methods provided in IRAF. The spectra were bias subtracted and divided by a flat-field frame (dome flat-field). Illumination corrections along the slit were found to be negligible. Cosmic ray events were removed. The spectra were calibrated in wavelength using comparison spectra of a CuAr arc taken before and after each object. Sky lines were carefully subtracted and the spectra corrected for atmospheric extinction with the aid of mean extinction coefficients for the AAO. Molecular bands due to atmospheric absorption were removed separately from all the spectra where they were evident. The bands were modeled appropriately for each frame, using the spectra of different standard stars taken with the same slit width as the one used for the target.

For each night, grating and grating angle, we built a mean response curve from the standard stars observed that night with the same filter and wide slit. Each target frame was flux calibrated with the corresponding response curve. The spectra were also corrected for Galactic reddening, E(B-V)=0.04, value based on Burstein and Heiles (1984) maps, using the empirical selective extinction function of Cardelli et al. (1989).

Both IRAF and STARLINK (DIPSO) routines were used to measure the emission line fluxes. For the blends, decomposition procedures were used in STARLINK (DIPSO), fitting several Gaussians at the expected positions of the components. As the number of mathematical solutions is very large, we applied the-

Table 2. Log of the spectroscopic observing run

Central λ	Grating	Exp time	Spectral range	Resolution (Å)	Seeing (")	Slit width (")
4600	1200V	6000	4210-5030	1.7	0.6	1.5
5800	600R	6000	4990-6590	3.3	1.0	1.5
6164	1200V	5400	5760-6580	1.5	0.6	1.5
8300	600R	3600	7520-9130	3.3	1.0	1.5

oretical constraints when necessary (like fixed ratios between line fluxes or separation in wavelength). In this way, we constrainted the range of solutions to a much smaller space where the resulting models have physical meaning. More details on the fitting procedures will be given in Sect. 3.6.

3. Analysis and results

3.1. The optical morphology

The raw and reconstructed [OII]+continuum images show complicated structures of line emission, which bear little resemblance to conical shapes expected in the case of anisotropic illumination of homogeneously distributed gas by a hidden AGN (see Fig. 1, top panels). The images show that the gas is distributed in clumps and filaments. This is observed in many radio galaxies and is likely to be due to the original inhomogeneous distribution of the gas in the early type host galaxy (Tadhunter 1990).

The main body of the galaxy shows a double structure in [OII]. A dark band defines two regions: one of them is coincident with the optical continuum nucleus, while the other — named ARM in Fig. 1, top left panel — is situated ∼5 arcsec (∼25 kpc) to the NE of the optical continuum nucleus. The separation between these two components is clearer in the bottom-right panel in Fig. 1. This double structure is not visible in the continuum image (Fig. 1, bottom-left panel).

Structures of clumpy gas are spread around the main body of the galaxy. An interesting feature is the filament extending towards the south (named "SF", for southern filament, in Fig. 1): it is a narrow, clumpy emission line feature which extends to a maximum radial distance of ∼17 arcsec (∼84 kpc). We believe that this component lies at the same redshift as the radio galaxy because it appears only in the [OII]+continuum images and not in the continuum images. The projected thickness of this arc is ∼6 arcsec (∼30 kpc). The bright blob (feature "B" in Fig. 1) could be connected with this southern filament.

An inverted S-like or arc-like feature is seen to the E at a projected distance of ∼19 arcsec (∼ 94 kpc) (feature "C"). Although this feature bears some resemblance to the bright emission line arc circumscribing the radio lobe in PKS 2250-41 (Clark et al. 1997a), in this case the filament lies significantly to the east of the eastern radio lobe (Fig. 1, bottom and see below). The astrometry was done using several stars in the frame, for which the positions were accurately known. The astrometry was mainly limited by the error on the radio and optical reference system (∼1 arcsec).

There is an interesting object in the field which is worth mentioning. The galaxy named 'A' in Fig. 1 could belong to the same system as PKS 1932-464, but we do not know its redshift. Spectroscopy of the object will provide the answer. The continuum image suggests the presence of two spiral arms, while the [OII]+continuum image reveals more chaotic structures.

3.2. The radio structure

The radio images of PKS 1932–464 at two of the four observed frequencies are shown in Fig. 2 (top). The 8.6 GHz image represents the highest resolution obtained — the image at 5.8 GHz looks very similar to this — while the 2.3 GHz image shows the morphology of the source at intermediate resolution (the 1.3 GHz image is very similar).

It is clear that the radio morphology of PKS 1932–464 is typical of Fanaroff-Riley type II radio sources, with bright hot-spots in the lobes. No jet structure has been observed. The two lobes are situated asymmetrically compared to the optical nucleus (marked as a cross in Fig. 2). The western lobe is at a projected distance of $\sim$ 11 arcsec ($\sim$ 54 kpc) from the optical nucleus of the galaxy whilst the eastern lobe is $\sim$ 7 arcsec ($\sim$ 35 kpc) from the nucleus.

At 8.6 GHz, the W side mainly shows the hot-spot that appears to be only slightly resolved. On the E side, together with the hot-spot, we can also see low-brightness, extended structure reaching back towards the optical nucleus. At 2.3 GHz, also the W lobe shows an extension toward the optical nucleus.

At 8.6 GHz, we can distinguish a core component between the lobes although it does appear to be offset (by $\sim$ 1.2 arcsec) from the position of the optical nucleus (see Fig. 2). Such an off-set is inside the range we expect given the uncertainty on the astrometry of the radio-optical frames. If we assume that the unresolved radio component is the core, we get a radio flux density of $S_{\rm core}^{\rm 8GHz} \sim 9$ mJy.

Values for the flux densities of the different components at different frequencies are given in Table 3.

3.3. Radio polarization

The values of the mean fractional polarization m in the lobes are given in Table 3. In Fig. 2 are shown the polarization vectors, whose length is proportional to the fractional polarization and whose position angle is that of the electric field, superposed on the intensity contour maps at both 2.3 and 8.6 GHz.

Assuming negligible Faraday rotation at 8.6 GHz (see below) the electric field in PKS 1932–464, is distributed radially at the edge of the lobes (i.e. the projected magnetic field follows

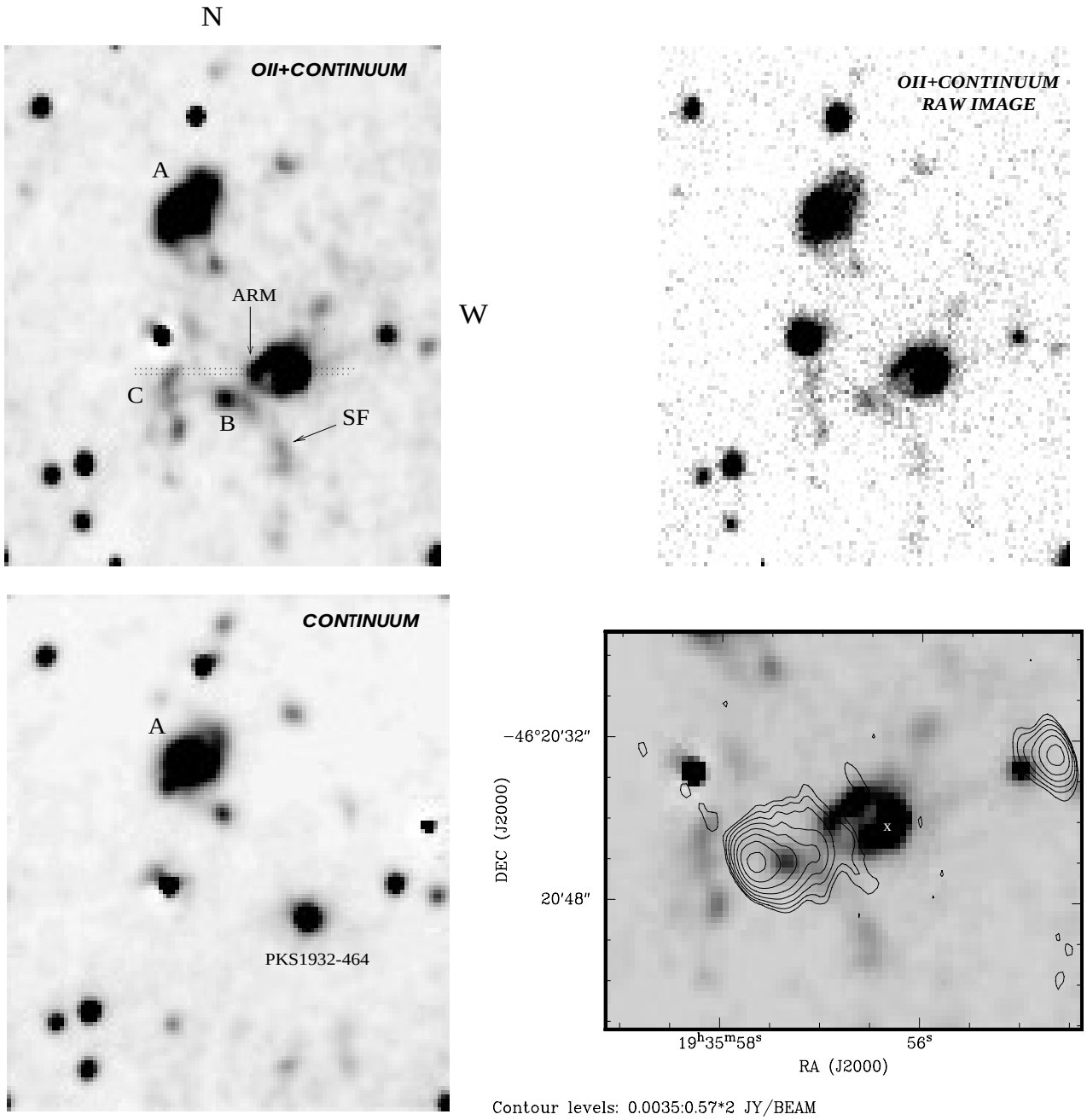

Fig. 1. Top-left: [OII]λ3727+continuum image, deconvolved with Lucy's algorithm. Top-right: Raw image. Most of the diffuse clumpy features surrounding the galaxy are pure line emitting regions. They do not appear in the continuum image (bottom-left), which has been deconvolved to the same spatial resolution. The slit position used for spectroscopy is shown in the top-left [OII]+continuum image. The pixel size in these images is 0.61 and the field is $\sim$65 arcsec E-W and 75 arcsec N-S. Bottom-right: Radio contours (5.8 GHz) overplotted on the [OII]+continuum image. The field is $\sim$50 arcsec E-W and 45 arcsec N-S.

the edge of the lobe) as shown in Fig. 2. This kind of structure is commonly seen in powerful radio galaxies. The structure of the projected magnetic field in the inner regions of the E lobe is more complex; a sharp change in position angle is visible (both at 8.6 and 2.3 GHz) in the W lobe between the edge of the lobe and the regions closer to the nucleus. There is also weak evidence of a 90° discontinuity in the E lobe at the transition from lobe to "bridge" (i.e. region closer to the nucleus).

Although some caution is required because of the different beam sizes, Table 3 shows that the W lobe is relatively strongly polarized ($>$ 10%) at every frequency, with a tendency for the fractional polarization to increase at high frequencies (where the effects of the beam smearing are also smaller). On the other hand, the E lobe shows a significant polarization only at 5.8 and 8.6 GHz. The percentage of polarization drops very sharply at the lower frequencies. This may be due to beam smearing

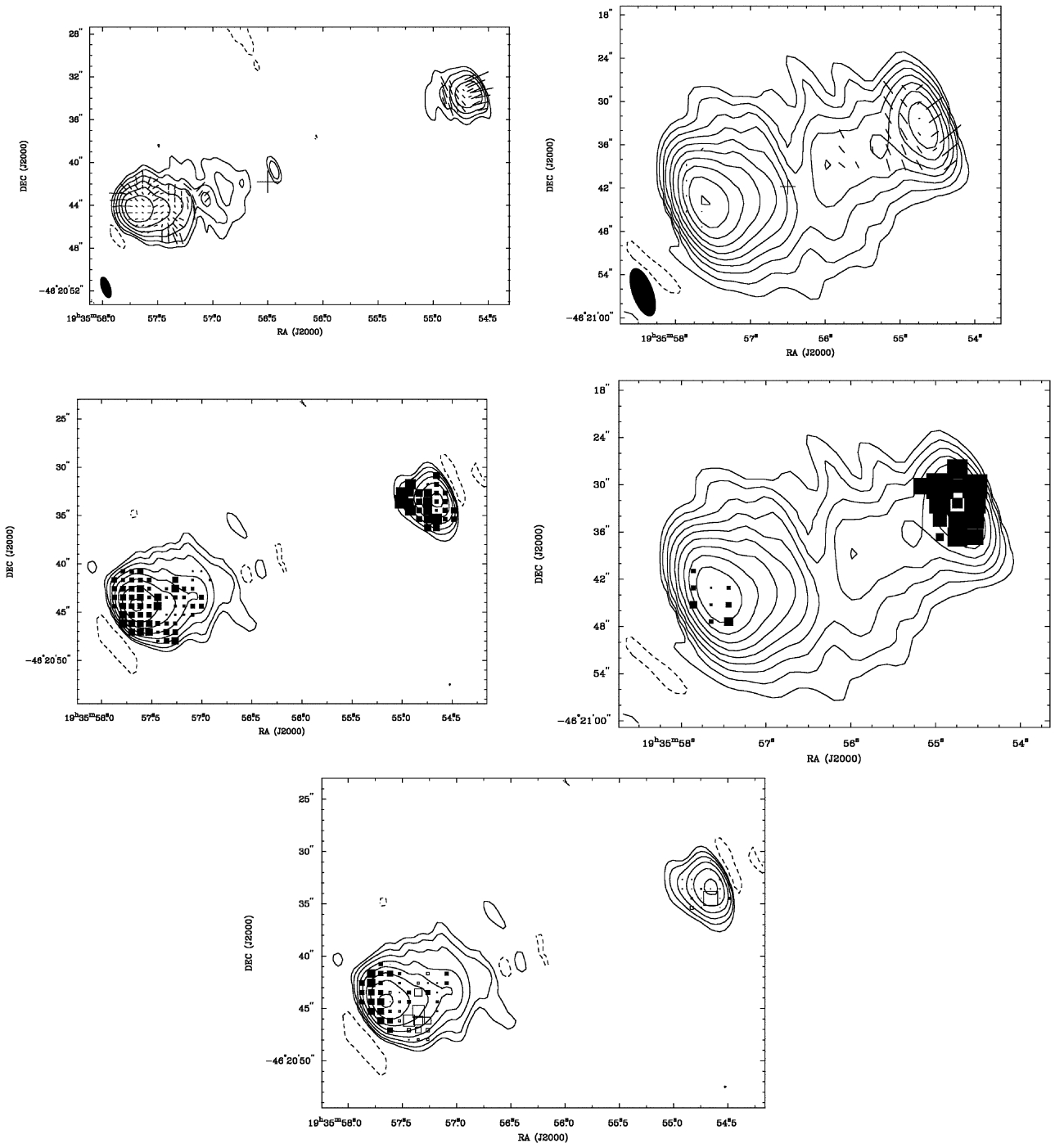

Fig. 2. Top-left: Radio contours of the total intensity at 8.6 GHz with superposed vectors whose length is proportional to the fractional polarization and whose position angle is that of the electric field. The contour levels are -1, 1, 2, 4, 8, 16, 32, 64, 128, 256, 512, 1024 $\times$ 4 mJy beam^{-1}. Top-right: Radio contours of the total intensity at 2.3 GHz with superposed electric field vectors. The contour levels are -1, 1, 2, 4, 8, 16, 32, 64, 128, 256, 512, 1024 $\times$ 4 mJy beam^{-1}. Middle-left: depolarization between 5.8 and 8.6 GHz. Smaller squares represent smaller D values (stronger depolarization). Square sizes range between D =0.19 (small squares) and 2.4 (large squares). Middle-right: depolarization between 2.3 and 5.8 GHz. Square sizes range between D =0.06 (small squares) and 1.6 (large squares) Bottom: Faraday rotation between 5.8 and 8.6 GHz. Filled squares are positive value of the rotation, open squares negative values.

Table 3. Radio parameters

Freq.	Total Flux	W lobe		E lobe	
		I(Jy)	m(%)	I(Jy)	m(%)
1.3 GHz	12.21	2.11	10.8±1.2	9.90	0.9±1.3
2.3 GHz	7.05	1.23	12.9±1.3	5.66	0.9±1.1
5.8 GHz[a]	2.50	0.32	17.9±1.7	2.11	6.6±0.7
5.8 GHz[b]	–	0.38	14.7±1.5	2.18	4.2±0.5
8.6 GHz[c]	1.60	0.24	19.3±2.5	1.30	10.0±1.4
8.6 GHz[d]	–	0.24	18.1±1.8	1.34	8.6±1.0

[a] full resolution (3.0x2.4 arcsec beam size)
[b] same resolution as the 2.3 GHz
[c] full resolution (2.0x0.8 arcsec beam size)
[d] same resolution as the 5.8 GHz

and therefore, in order to reduce the effects of different beam size and investigate polarization and spectral index, we have produced an 8.6 GHz image with the same resolution as the 5.8 GHz image, and we have also carried out a similar procedure at 5.8 GHz and 2.3 GHz. We lowered the resolution of the higher frequency by a Gaussian weighting function (taper) applied to the visibilities. The values of the fractional polarization obtained from the images with "degraded" resolution are also given in Table 3.

Using the images with matched beam size we have estimated the depolarization ratio between two frequencies, defined as $D = m_{\nu_1}/m_{\nu_2}$ with ν_1 and ν_2 the lower and higher frequency respectively. We find depolarization values of 0.79 for the E lobe and $\sim$ 1 (i.e. no depolarization) for the W lobe between 5.8 and 8.6 GHz. Between 2.3 and 5.8 GHz we find a D = 0.23 (strong depolarization) for the E lobe and D = 0.89 for the W lobe. This confirms the strong depolarization in the E lobe when we go to lower frequencies. Fig. 2 (middle) shows the depolarization values superposed on the 5.8 and 2.3 GHz total-intensity contours. The size of the boxes is proportional to the value of the depolarization: big boxes represent value close to 1 (i.e. weak or no depolarization), small boxes represent values close to zero (i.e. strong depolarization).

In summary, no strong depolarization is found between 5 and 8 GHz in PKS 1932–464 and only a marginal assumetry in the depolarization is observed (at these frequencies) between the two lobes. However, a strong depolarization is present in the E lobe of PKS 1932–464 for lower frequencies, i.e. between 2.3 and 5.8 GHz. This is different from the results obtained for PKS 2250-41 (Clark et al. 1997a) where, even at high frequencies, a large depolarization is observed in the radio lobe close to the EELR.

From our data, we can only estimate the Faraday rotation measure (RM) between pairs of frequencies (those with the same resolution). The RM is defined as $\chi(\lambda^2) = \alpha + RM\lambda^2$, where α is the intrinsic position angle and χ the apparent position angle at the λ of the observations. Since the position angles are ambiguous by π, the RM calculated from only two frequencies are ambiguous by $\pm n\pi$ rad m^{-2}.

Between 5.8 and 8.6 GHz we find a small RM in the W lobe. The median RM is ~ -9 rad m^{-2} but ranging between –14 rad m^{-2} in the eastern part to 35 rad m^{-2} in the western side of this lobe. In the E lobe the RM shows a wider range of values from $\sim$ 181 rad m^{-2} in the eastern side to ~ -107 rad m^{-2} in the western part. The RM between 2.3 and 5.8 GHz shows similar values in the W lobe with $RM \sim$ 19 rad m^{-2} (indicating that no π ambiguity should be present) but it is too uncertain in the E lobe.

The depolarization and the RM observed in radio galaxies are commonly attributed to the effect of an inhomogeneous, unresolved, foreground screen, which rotates the polarization position angle randomly across the synthesized beam (the effective vector sum of the radiation is thus depolarized). Indeed, by using the formula in Clark et al. (1997), we find that an RM gradient of only 25 rad m^{-2} arcsec^{-1} is required to cause the observed depolarization ratio to fall to a value of $D \sim 0.24$ between 2.3 and 5.8 GHz (13 and 6 cm). Thus, the observed depolarization seems to be compatible with an unresolved RM fluctuation (caused by a Faraday screen anywhere along the line of sight) across the synthesized beam causing the electric vector to rotate across the beam.

Although the identity of the depolarizing medium is uncertain, it is possible that at least some depolarization is associated with the warm emission line gas. This is supported by the fact that the region of highest depolarization in the eastern lobe is coincident with the position of knot B in the emission line image (see Fig. 1).

Finally, we also computed an image of the spectral index (α, defined as $S_\nu \propto \nu^\alpha$), between 5.8 and 8.6 GHz. We find $\alpha = -1.30$ for the E lobe, $\alpha = -0.67$ for the W lobe.

3.4. The spatial distribution of the emission lines

The position of the slit is shown in Fig. 1 (top-left panel). The slit – aligned along PA 270 – contains the optical nucleus but is rotated with respect to the radio axis so that it does not contain the main radio features (hot spots).

We have examined the spatial distribution of the emission line fluxes by extracting 1-dimensional spatial cuts from the 2-dimensional frame, adding the pixels along the spectral direction which contain the line emission, and subtracting a spatial profile of the continuum obtained in a similar way. This procedure was carried out for [OII]λ3727, Hβ, [OIII]λ5007, [OI]λ6300 and Hα+[NII]λ6583.

The spatial distribution of the lines is shown in Fig. 3 for [OII]λ3727, Hβ, [OIII]λ5007, [OI]λ6300 and Hα+[NII]λ6583.

The pure line spatial profiles reveal three main spatial regions: the nuclear region (extending to radial distances of $\sim$3 arcsec or 15 kpc on both sides of the nucleus), the *inner* EELR (extending to radial distances of $\sim$10.5 arcsec or 52 kpc to the East of the nucleus) and the *outer* EELR (extending to a maximum radial distance of $\sim$23 arcsec or 113 kpc to the East of the nucleus). The outer EELR coincides with the arc like feature mentioned in Sect. 3.1 (feature "C" in Fig. 1), which lies outside the E radio lobe. The inner EELR corresponds to the extended gas near the main body of the galaxy, also mentioned in

Table 4. Line fluxes relative to Hβ for the three spatial regions considered in the text: the nuclear region, the inner EELR and the outer EELR. Hβ flux is given in units of ergs s^{-1}cm^{-2}

	Nucleus	Inner EELR	Outer EELR
Flux(Hβ)	(1.17±0.04)×10^{-15}	(2.9±0.3)×10^{-16}	(1.4±0.2)×10^{-16}
[NeV]λ3426	0.35±0.03	$\leq$ 0.16	$\leq$0.21
[OII]λ3727	4.9±0.2	7.6±0.9	4±1
[NeIII]λ3869	0.74±0.05	0.8±0.2	0.9±0.3
[Ne III]+Hλ3967	0.22±0.03	0.4±0.1	0.5±0.2
Hδ	0.21±0.04	$\leq$ 0.16	$\leq$0.13
Hγ	0.39±0.08	0.5±0.1	$\leq$0.30
[OIII]λ4363	0.09±0.03	0.2±0.1	$\leq$0.46
HeIIλ4686	0.15±0.05	0.2±0.1	0.4±0.2
Hβ	1.00	1.00	1.00
[OIII]λ5007	6.7±0.3	4.7±0.6	10±1
[NI]λ5199	0.17±0.04	0.2±0.1	$\leq$0.06
[OI]λ6300	1.01±0.08	0.6±0.2	$\leq$1.03
Hα	3.3±0.2	3.6±0.4	1.8±0.6
[NII]λ6583	1.8±0.1	1.9±0.3	0.4±0.2
[SII]$\lambda\lambda$6716+6732	1.9±0.1	2.3±0.5	$\leq$1.31

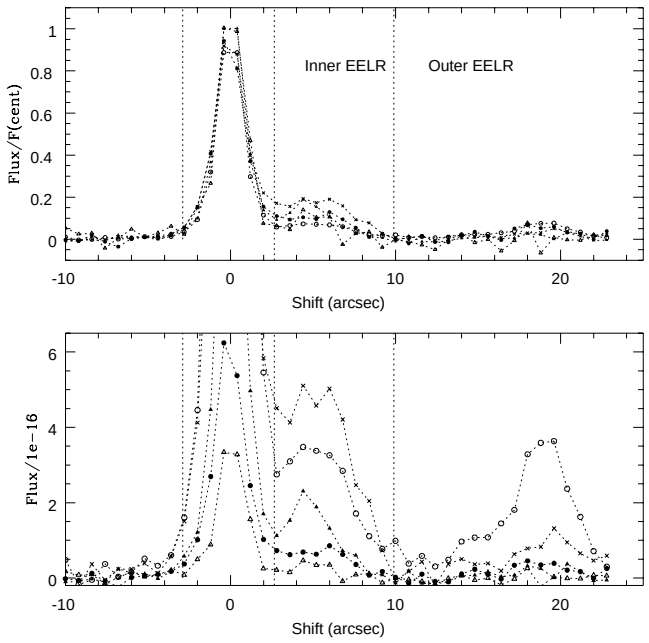

Fig. 3. Integrated (in λ) spatial profiles of the lines [OII]λ3727, [OIII]λ5007, [OI]λ6300, Hβ, Hα+[NII]λ6583. Top-panel: For every line, the flux has been normalized to the value at the position of the continuum centroid. Bottom-Panel: The fluxes have been divided by 10^{-16} to highlight the differences in the spatial profiles of the different lines. The three spatial regions considered (see text) have been separated by vertical lines. Open circles - [OIII]λ5007; crosses - [OII]λ3727; solid circles - Hβ; solid triangles - Hα+[NII]; open triangles - [OI]λ6300.

Sect. 3.1 and named "ARM" in Fig. 1. The spatially integrated spectra for each region are shown in Fig. 4.

The peak of the emission lies in the nuclear region for all the lines. The inner EELR emits stronger lines than the outer one, except for [OIII] which is stronger in the arc. [NII]+Hα show a much steeper distribution than the other lines, with the peak also closer to the nucleus.

3.5. The line ratios and ionization gradient

Table 4 shows the line fluxes (normalized to Hβ) for some interesting lines. The line ratios have not been corrected for reddening due to dust internal to the galaxy PKS 1932-464. The highest measured Balmer decrements (3.6±0.4) indicate that E_{B-V} <0.23, which is consistent with no significant reddening within the errors.

The spatial variation of the ionization level of the gas is presented in Fig. 5, where we plot [OII]λ3727/[OIII]λ5007 and [OIII]λ5007/Hβ vs. projected distance from the nucleus.

The spectra containing the three main emission lines where observed on the same night, with similar seeing and same slit width and position. Therefore, we are confident that the [OII]/[OIII] measurements are reliable. The agreement with the [OIII]/Hβ ratio behaviour supports this point.

We find the ionization decreases moving outwards across the *inner* EELR (and E radio lobe), where it presents a minimum and then rises to high values in the *outer* EELR.

3.6. The kinematics

A close inspection of the 2-D frames shows a clear difference in the kinematics of the gas in the inner and the outer EELR (see Fig. 6). The inner EELR shows two distinct spectral components (A and B in Fig. 6), which are evident in all lines, while the emission lines of the outer EELR are apparently simple. The two spectral components in the inner EELR are spatially separated: component A lies closer to the nucleus and is redshifted with respect to component B. The peaks of the emission are separated by ∼2.4 arcsec (∼12 kpc) in projection. Close inspection of the 2-D frame reveals a rather sharp cut between these components in the spatial direction. This suggest that we are observing

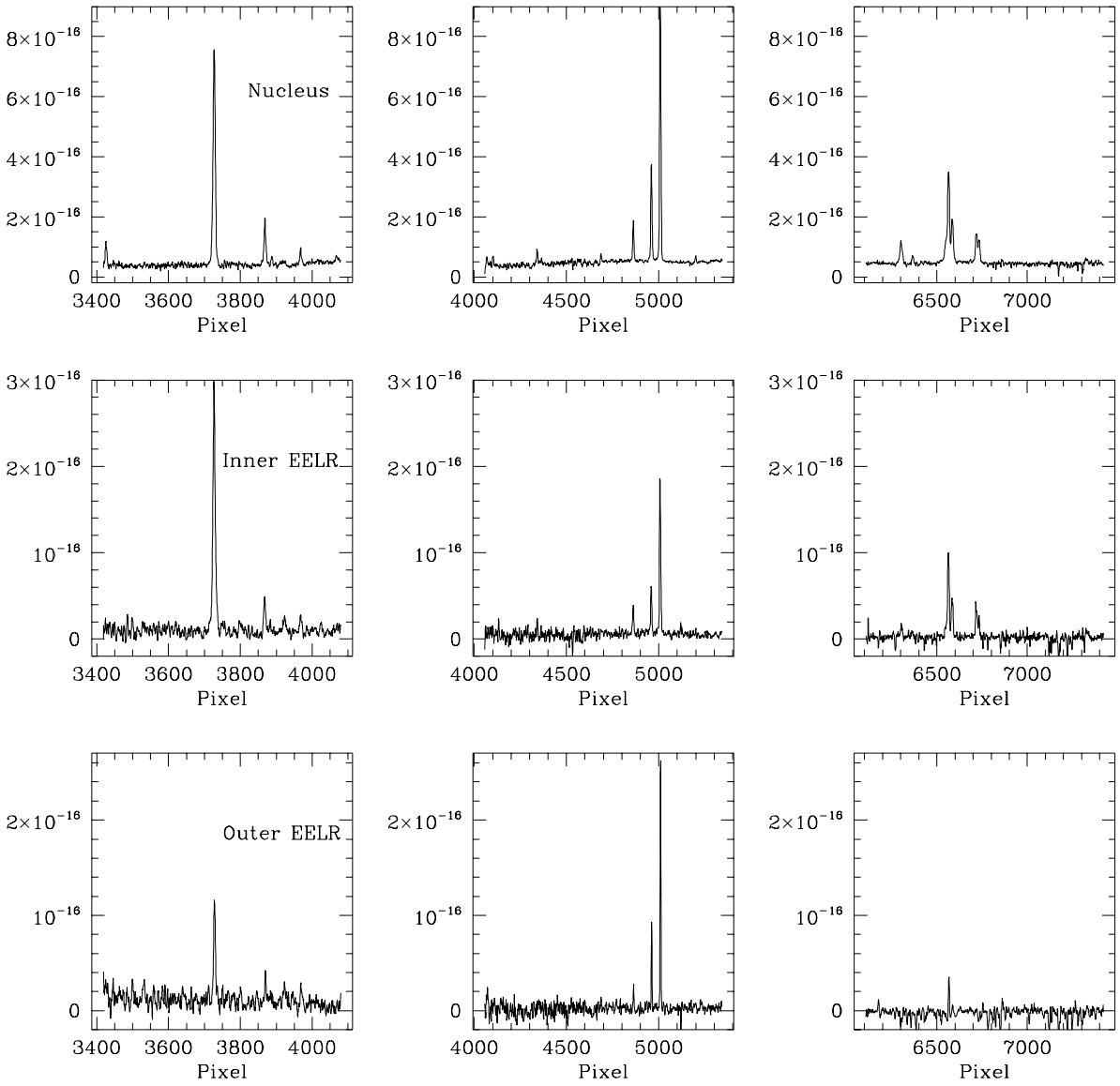

Fig. 4. The spectra of the three spatial regions revealed by the pure emission spatial profiles. The upper panels show the nuclear spectra. The middle panels show the spectra of the inner EELR, which corresponds to the extended gas, near the main body of the galaxy, named "ARM" in Fig. 1. The bottom panels show the spectra of the outer EELR, which coincided with the arc-like shape feature (named "C") in Fig. 1.

two spatially disconnected components, rather than a mixture of gases with different kinematic properties.

We have studied the spatial variation of the line widths and the velocity shifts with respect to the nuclear emission. We have also compared the behaviour of the different lines for every spatial position.

In order to do this, we isolated 1-D spectra from every spatial pixel. We then fitted the line profiles with simple Gaussians, fixing constraints to obtain fits with physical meaning (e.g. the theoretical flux ratios). The center of the Gaussian were taken as the central wavelength of the line and the FWHM as the measured FWHM of the line. The measured line widths were corrected for instrumental broadening.

The results are shown in Fig. 7. Each symbol represents a different line. All lines were resolved at every spatial pixel, except in a few exceptional cases, which will be indicated by arrows (upper limits) in the plots. Where the lines were too faint, several pixels were binned. This is indicated by a thick dashed horizontal line, showing the pixels which were added. The main results are as follows.

The velocity field

The velocity field along PA270 (Fig. 7, top) shows no definite pattern and the radial velocity range covered is $\sim$400 km s^{-1}, which is comparable with the values measured in other radio galaxies with no signs of jet-cloud interactions (e.g. Tadhunter et al. 1989, Baum et al. 1990).

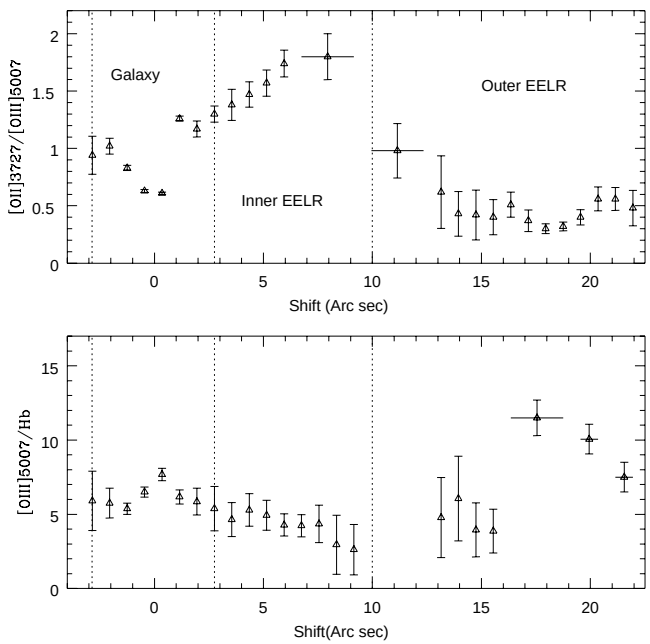

Fig. 5. The ionization gradient: Spatial variation of the [OII]λ3727/[OIII]λ5007 and [OIII]/Hβ line ratios. Where the lines were too faint, several pixels were binned spatially. This is shown by horizontal lines in the plots, which indicate the pixels which were added.

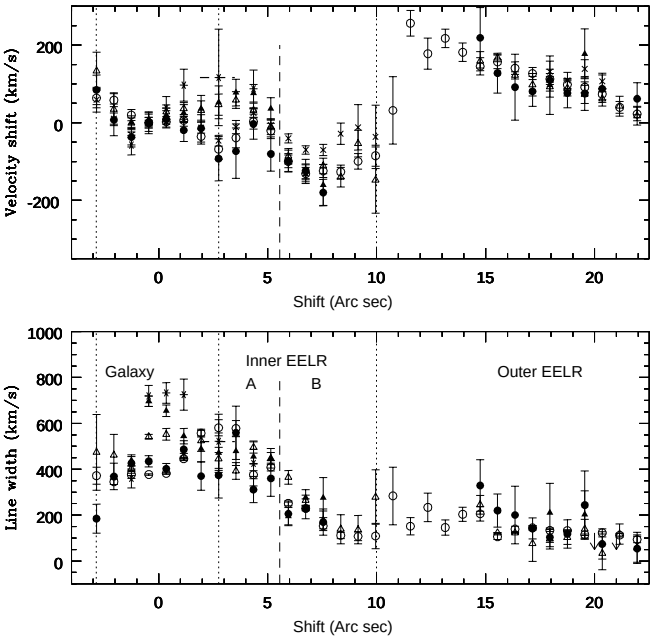

Fig. 7. Variation in the radial velocity shifts (top) and line widths (bottom) along PA 270. Open circles - OIIIλ5007; crosses - [OII]λ3727; solid circles - Hβ; open triangles - Hα; solid triangles - [NII]6583; stars - [OI]λ6300. Line widths for [OII] have not been plotted; due to the contribution of the doublet components the measured widths could be misleading. [OI] line might be contaminated by the [SIII]λ6312 line. The three main spatial regions (see text) are separated by dotted lines. The long dashed line marks the separation between the two velocity components A and B seen in the inner EELR.

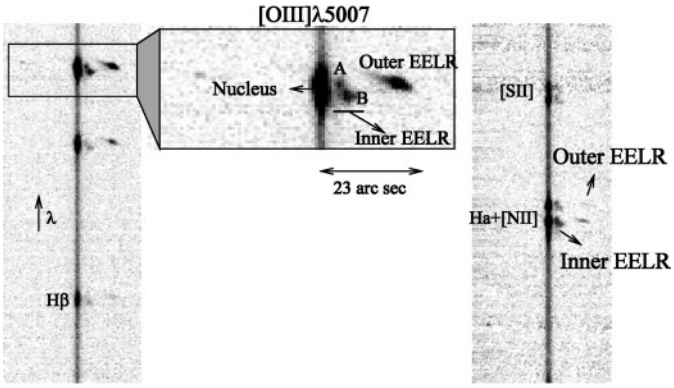

Fig. 6. Left: 2-D spectrum showing [OIII]$\lambda\lambda$5007,4959 and Hβ (red is up). Middle: Zoomed [OIII]λ5007 region. Right: Red spectrum showing Hα+[NII] lines and the [SII] doublet (top). The different kinematics in both EELR is evident: the inner EELR shows split components while the outer one shows narrow simple lines.

The diagrams reveal that the nuclear region, the inner EELR and the outer EELR are kinematically distinct.

The inner EELR shows a velocity curve which is a continuation of the velocity field in the nuclear region. However, as expected from Fig. 6, there is a jump (clear in the [OIII] line) in the transition region between the inner and outer EELR (at $\sim$10.5 arcsec from the nucleus). Components A and B of the inner EELR present different velocity shifts with respect to the nucleus. At the spatial peak of intensity, B is redshifted $\sim$150 km s^{-1} with respect to the nucleus. Line emission from the peak of intensity of component A reveals a very small velocity shift in the line of sight with respect to the nucleus.

The *outer* EELR shows velocity shifts which decrease outwards from $\sim$250 km s^{-1} to $\sim$25 km s^{-1} in the region most distant from the nucleus. This is also seen in the 2D frame (Fig. 6), where a tail of [OIII] emission extends towards the nucleus.

Both the inner and outer EELR show on average a similar velocity shift ($\sim$100 km s^{-1}) for the lines with respect to the nuclear region, but with opposite signs.

The line profiles

As a first approximation, we fit simple Gaussians for every line and at every spatial position. Large widths are measured for [OI]λ6300, [NII]λ6583 and Hα in the nuclear regions of the galaxy compared to [OIII]λ5007 and Hβ in the same region. The large widths measured for [NII] and Hα could be due to the existence of an underlying broad Hα component, which we have not taken into account. On the other hand [OI]λ6300 could be contaminated with the line [SIII]λ6312. This is supported by the fact that the width of the [OI]λ6364 line is $\sim$480 km s^{-1}, similar to the values measured for [OIII] λ5007 and Hβ. The nuclear spectrum deserves a separated study and we will analyze it in detail in the next section.

The *inner* EELR emits lines with split components (see Fig. 6) which reveal two gaseous components moving in dif-

Table 5.

Line	Wavelength	FWHM km s^{-1}	v$_{shift}$ Hα_{B-N} km s^{-1}
[NII]λ6543	6549.2±0.3	520±80	
Hα_N	6563.4±0.4	510±70	
[NII]λ6583	6584.2±0.2	520±80	
Hα_B	6562±2	2400±200	-70±80

ferent ways: component A (closer to the nucleus) shows similar line widths ($\sim$450 km s^{-1}) and radial velocity ($\sim$0 km s^{-1}) to the nuclear region. Component B is blueshifted by $\sim$150 km s^{-1} and shows narrower lines ($\sim$200 km s^{-1}). This further supports the idea that we are observing two kinematically distinct components in the inner EELR.

The broader lines measured in component A of the inner EELR could be due to a contribution to the line profile from a spatial extension of component B towards the nucleus. We have investigated whether the line profile of component A can be fitted by two narrow components, rather than a broad one. The result indicates that the best fit is, indeed, obtained with a single broader component.

The line widths are narrow in the outer EELR region (but still resolved) compared to the inner EELR, showing $\sim$200 km s^{-1} (FWHM), similar to component B of the inner EELR (see Fig. 7).

Within the errors, all lines in the extended emission line regions show very similar widths and velocity shifts at every spatial position.

The nuclear spectrum

A detailed analysis of the nuclear continuum spectrum by Dickson et al. (1997) reveals a significant UV continuum excess compared with normal early-type galaxies. Possible origins for the UV excess include: scattered AGN light, the light from young stellar populations in the host galaxy, and direct AGN light. However, the low polarization measured for the UV continuum ($P < 1.6\%$, Dickson et al. 1997) rules out the idea that the UV continuum is dominated by a scattered AGN component. In this section we search for broad permitted lines in the nuclear spectrum to gauge whether there is a significant contribution from direct, rather than scattered, AGN light.

Attempts to fit the [NII] + Hα blend using only narrow components provide an unsatisfactory fit to the wings of the blend. We find that the best fit to the blend requires a broad component to Hα with velocity width 2400$\pm$200km s^{-1} shifted by 70$\pm$80 km s^{-1} with respect to the narrow component. The results of the fit are presented in Table 5 and in Fig. 8. The detection of broad Hα indicates that PKS 1932-464 is a broad line radio galaxy (BLRG), albeit with relatively weak broad lines. Combined with the low UV polarization this result supports the idea that there is a significant contribution from direct AGN light in this object.

The best fit to Hβ line requires only a narrow component, broad wings are not detected. Taking into account the properties of the broad component of Hα, we have checked whether the corresponding broad component to Hβ should be detectable. Our predictions indicate that a broad component to Hβ with the same velocity width as broad Hα and a flux such that Hα_{broad}/Hβ_{broad} $\sim$3 would be undetectable.

In comparison with other BLRG, the nucleus of PKS 1932-464 has a relatively weak radio core ($R_{8.6GHz}$ = $S_{\rm core}/S_{\rm ext} <$ 0.006, see also Morganti et al. 1997), although its X-ray luminosity ($L_x = 6 \times 10^{43}$, Siebert et al. 1996) is comparable with other BLRG in the sample of southern 2Jy radio sources (Tadhunter et al. 1993).

4. Discussion

4.1. The optical morphology and the connection with the radio structures

The optical morphology shows complicated structures of ionized gas, including narrow filaments and arcs. Some of these structures may represent the remains of tidal tails resulting from interactions with other galaxies, while other features could be the result of interactions between the radio structures and the ambient gas. It is unlikely, however, that all the EELR are currently interacting with the radio plasma, since the filament to the south lies well away from the radio axis, and the arc-like feature to the east lies outside the eastern radio lobe.

As mentioned in Sect. 3.1 the main body of the galaxy shows double structure in [OII]λ3727. It is interesting to note that a complex morphology in the central nuclear region has been found in other radio galaxies, including 3C171 (Clark et al. 1997b), and many of the targets observed during the HST Snapshot Survey of 3CR radio galaxies (Koff et al. 1996). In some cases it is clearly due to the presence of an obscuring dust band. The fact that the double morphology is not apparent in the optical continuum image of PKS 1932-464 (Fig. 1, bottom-left) suggests that a) the structure is not due to dust, but rather due to a lack of emission line material or b) the continuum emission is concentrated in a more compact region in such a way that the dust band does not obscure it. In such a situation, the dark band would be apparent in the line+continuum image, but not in the pure continuum image.

Another possibility is that the radio jet in its passed through the extended gas has hollowed a channel (eg. Jackson et al., 1993)). However, the direction of this channel in PKS 1932-464 is rotated with respect to the radio axis and this interpretation appears unlikely (see Fig. 1, bottom-right). Alternative possibilities will be discussed later.

The morphology of feature "C" in Fig. 1 (the arc-like shape structure) is reminiscent of the radio galaxy PKS 2250-41, where the western arc of line emission lies just beyond the western radio lobe. There are reasons to believe that in PKS 2250-41 the W radio lobe is confined and constrainted by the line emitting gas (see detailed discussion in Clark et al. 1997a). In PKS 1932-464, the physical connection is not so clear. From the overlap of the radio and optical images, the hot spot lies $\sim$4 arc sec ($\sim$20kpc) from the inner part of the arc. Considering possible errors in astrometry, if we assume that the radio core and the

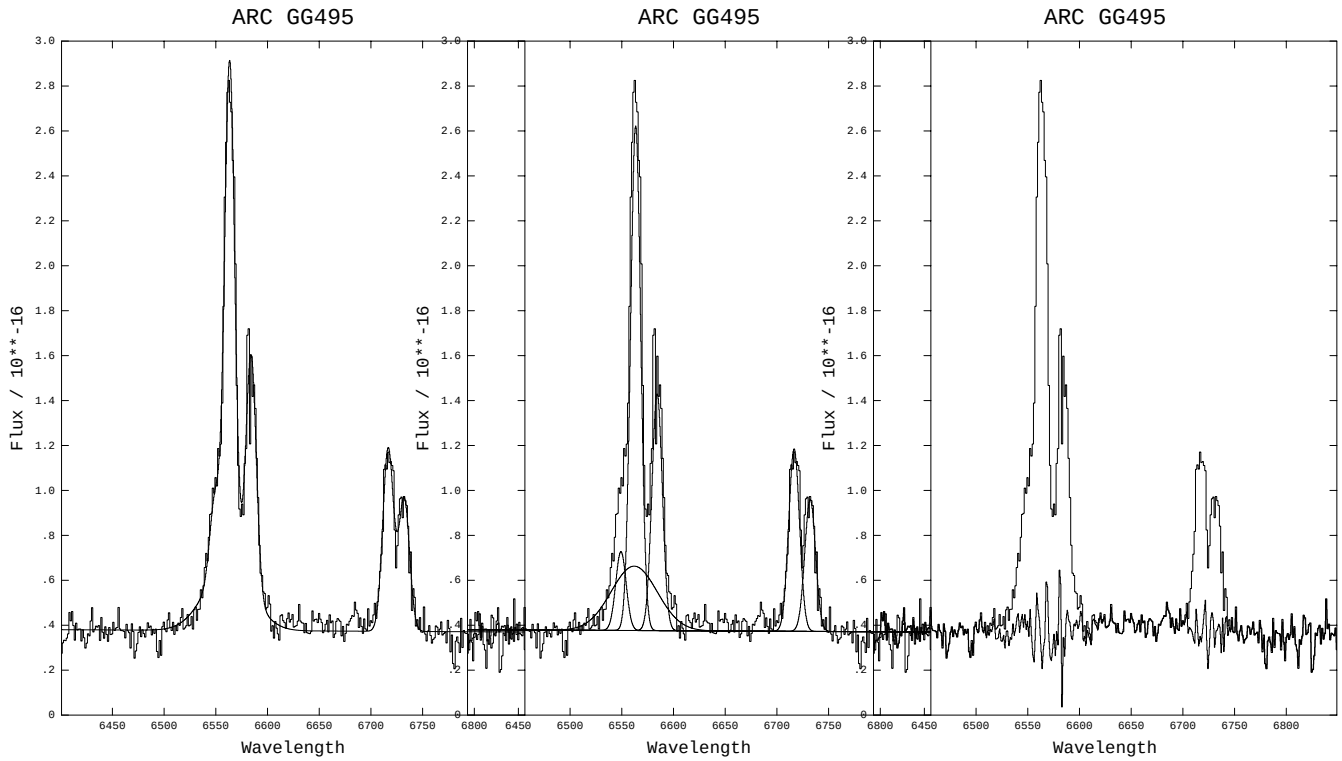

Fig. 8. Fit to Hα+[NII] and [SII]. Left: Data and fit. Middle: Data and individual components of the fit. Rigth: Data and residuals.

optical nucleus are at the same location, this distance is $\sim$14 kpc in projection. There is also some offset in between the arc and radio hotspot in PKS 2250-41, the offset distance is smaller in this object ($\sim$10 kpc). Another example is provided by Cyg A. Carilli et al. (1994) detected an arc of discontinuous RM roughly concentric with a hotspot. This might be a bow shock formed after the material is compressed by the shocks produced by the advancing hot spot. The projected distance from the bow shock to the hot spot is $\sim$4.5 kpc.

The arc in PKS 1932-464 presents some differences with the arc in PKS 2250-41 which make less clear its physical association with the radio lobe: the line widths are smaller and the ionization state much higher.

4.2. PKS 1932-464 and the high redshift radio galaxies

Despite its relatively low redshift, PKS 1932-464 shares a number of characteristics with high z ($z > 0.7$) radio galaxies. In particular, McCarthy & van Breugel (1989) have shown the arm-length ratio (ratio between the distance of the two lobes from the core) for 3CR radio galaxies is strongly a function of redshift with the arm-length ratio increasing with redshift. The arm-length ratio observed in PKS 1932-464 is 1.56 that is typical of objects with $z > 0.7$ while at the redshift of PKS 1932-464 the typical ratio is 1.18. Moreover in high-z radio galaxies the extended emission lines are brighter on the side of the radio lobe closest to the nucleus (McCarthy & van Breugel 1989, Pedelty et al. 1989) and this lobe is also systematically more depolarized (Pedelty et al. 1989, Liu & Pooley 1991). These characteristics are also observed in PKS 1932-464. The arm-ratio asymmetry could have different causes but the most likely is that the propagation of the plasma jet is affected by an external medium which is inhomogeneously and asymmetrically distributed around the galaxy (McCarthy & van Breugel 1989, Pedelty et al. 1989) This scenario can also explain the higher depolarization in the lobe closer to the nucleus: this lobe would be the one more deeply embedded in the halo and therefore more highly depolarized.

The distribution of EELR in PKS 1932-464 is not such to explain the overall depolarization of the E lobe (i.e. they "cover" only part of the radio lobe). This supports that an external medium is responsible. If the warm gas (the gas in the EELR) traces the distribution of hot external ISM, we expect a denser (asymmetric) medium on the E side. This could explain the higher depolarization. This medium could be the hot halo mentioned above. Another possibility is that the hot ISM is distributed in a denser sheath around the lobes as proposed in the case of Cygnus A by Dreher et al. (1987).

We cannot exclude, however, that the EELR can still affect the depolarization on smaller scales (Pedelty et al. 1989) and explain some of the patchy distribution observed in the depolarization in PKS 1932-464. In PKS 1932-464 we note that the region of higher depolarization in the eastern lobe is coincident with one bright region of ionized gas, region B.

The radio sources in high-z objects are thought to show a particularly strong interaction between the radio plasma and the environment (e.g. McCarthy et al. 1987, Best et al. 1996). The fact that PKS 1932-464 as well as PKS 2250-41 (Clark et al.

1997a) look so similar to these high-z objects suggests that there are systems at low/intermediate redshift where we see situations *very* similar to the high redshift systems. The similarity must be in the environment. Together with other peculiarities, high-z radio galaxies show an excess of companion galaxies detected along the axes of the radio sources (Röttgering et al. 1996). Interestingly, both PKS 2250-41 and (possibly) PKS 1932-464 have a companion.

4.3. The line ratios and the emission line mechanism

The two main mechanisms which might be involved in the emission line processes are: a) photoionization by the hard UV continuum emitted by the central AGN, and b) high velocity radiative shocks which can influence the emission line processes due to the generation of a strong local UV photon field in the hot post-shock zone, which can ionize the surrounding medium both upstream and downstream. Moreover, the radiative cooling of gas behind the hot post-shock zone can also give rise to line emission.

The optical line ratios of PKS 1932-464 locate this object in the general trend defined by low redshift radio galaxies in the diagnostic diagrams involving optical lines (Robinson et al. 1987). However, the optical emission lines do not allow the discrimination between shock and AGN photoionization because the models overlap in their predictions of the optical line ratios.

In Sect. 3.5 we showed that the ionization level of the gas decreases outwards from the nucleus across the inner EELR and rises to high values in the outer EELR (see Fig. 5).

Can this behaviour be explained in terms of pure AGN photoionization? The decrease in the ionization level across the inner EELR is consistent with AGN photoionization: the AGN continuum is diluted at increasing distances from the nucleus (varying as $\sim 1/r^2$). For a gas density which decreases less steeply than $\sim 1/r^2$ we expect the ionization level to decrease because of the steeper drop in the number of ionizing photons compared to the number of atoms to be ionized.

However, the outer EELR shows a noticeably higher ionization level. In the frame work of pure AGN photoionization, this implies that the density must drop more rapidly that $\sim 1/r^2$ between the inner and the outer EELR. Another possibility is that projection effects mislead us. It is possible that what we have named inner EELR, is, indeed, more distant to the nucleus than the one we have called outer EELR. In this case, the high level of ionization observed in the outer EELR could be due to the higher density of ionizing photons. However, the projection factors would have to be extreme for this explanation to hold.

Can this behaviour be explained in terms of processes associated with shocks? The [OIII]/Hβ ($\sim$3-5) and [OII]/[OIII] ($\sim$1.5-2) ratios in the inner EELR indicate a very low ionization level. Such values are in good agreement with those observed in radio galaxies with jet-cloud interactions (Clark 1996). The low ionization state of the inner EELR is consistent with the compression effect of the jet shocks. It is interesting to note that in other objects with jet-cloud interactions a minimum in the ionization state is observed to be coincident with or just beyond the radio hot spots (for instance, 3C171, 4C29.30, ComaA: Clark 1997). In PKS 1932-464, this ionization minimum occurs well behind the radio hot spot, close to the inner edge of the E radio lobe. It is important to remember that the slit did not cross the radio hot spot where the main signs of interaction will occur. Therefore, we do not know whether the ionization level is even lower at this position. The low ionization level of the inner EELR suggests, independently of the mechanism (shocks or outflowing wind), that the gas has been compressed in this region.

As the gas in the outer EELR lies outside the radio source it is reasonable to think that it is ionized by the continuum emitted by the central AGN and/or by the strong UV continuum emitted by fast shocks. The [OIII]/Hβ ($\sim$10) and [OII]/[OIII] ($\sim$0.4) emission line ratios support this idea: they indicate a high ionization level which cannot be explained in terms of shocked gas which is cooling down, but rather gas which has not entered the shock and is being photoionized by a strong UV continuum.

4.4. The kinematics

As we mentioned before, the kinematical properties of the gas reveal the presence of two well differentiated EELR regions, coincident with the regions defined by the spatial line profiles (the inner and the outer EELR). Particularly interesting is the inner EELR. It presents split components and large line widths ($FWHM$ $\sim$450 km s^{-1}) which suggest that its kinematics has been perturbed. Line widths of this order are not as extreme as observed in some radio galaxies with jet-cloud interactions, such as 3C171 (Clark et al. 1997b), for which broader components ($FWHM$ $\sim$1000 km s^{-1}) are detected. However, it is interesting to remark that the lines are noticeably broader than those emitted in the outer EELR ($FWHM$ $\sim$200 km s^{-1}).

The fact that we do not detect extreme motions in the extended gas of PKS 1932-464 does not mean that the kinematics is not highly perturbed. The slit was not exactly aligned with the radio axis, where the most extreme motions are expected if the jet is interacting with the ambient gas. Moreover, it is possible that faster motions could be taking place perpendicular to the line of sight.

Other radio galaxies with jet-cloud interactions show a clear anticorrelation between line widths and the ionization state of the emitting ion. Low ionization lines are broader than high ionization lines (Clark et al. 1997b). This is observed also in supernova remnants and is attributed to the fact that low ionization emission lines are produced mainly in the shocked, compressed and accelerated gas, while the high emission lines are mainly a contribution of the non-shocked gas (Greidanus & Strom, 1992). The spatial distribution of the velocity shifts and line widths does not reveal this behaviour (Fig. 7) along PA270 in PKS 1932-464. We have checked if the spatially integrated spectra for the different spatial regions (outer EELR, and components A and B of the inner EELR) show this same behaviour. We found some differences among the lines emitted in component B of the inner EELR, with the low ionization lines being

broader than the high ionization lines. This effect, however, is likely to be due to a velocity gradient across the gaseous region.

5. PKS 1932-464: a jet-cloud interaction in a radio galaxy?

Clark et al. have studied a small sample of intermediate redshift radio galaxies which were already known to show clear evidence for jet-cloud interactions. This evidence comes both from spectroscopy and imaging. The targets show some special properties which are a consequence of the interaction between the radio jet and the ambient gas in the galaxy. Some of these properties have already been mentioned.

a) Striking correspondence between line emission and radio structures

b) Highly perturbed kinematics shown by complex emission line profiles: split narrower components (Δv $\sim$550km s^{-1}) and an underlying broad component ($FWHM$ $\sim$1000 km s^{-1}) are often observed.

c) Anti-correlation between line width and ionization state.

d) Association of ionization minima with shocked structures. The compression effect and maybe also shock ionization produce a drop on the ionization level of the gas.

Do we see any of these properties in PKS 1932-464?

a) The overlay of the radio and optical maps show that the outer EELR lies outside the radio structure and appears to circumscribe the E radio lobe. However, the large offset between the radio hotspot and the outer arc, the apparently quiescent kinematics of the emitting gas in this region (with narrow lines and simple profiles), and the high level of ionization, do not provide evidence for such an interaction and the observed properties of this gas could well be explained in terms of AGN illumination. The inner EELR lies well inside the radio structures and an interaction is plausible.

On the other hand, PKS 1932-464 shares many similarities with high redshift (z$>$0.7) radio galaxies: the radio lobe arm-ratio, radio depolarization and optical asymmetries. These similarities suggest that, as in high redshift radio galaxies, PKS 1932-464 lies in a rich environment which is interacting with the radio jet.

b) Our study of the kinematics of the EELR does not show extreme motions along PA270. However, the differences in the kinematic properties of the outer and inner EELR suggest that different mechanisms are influencing the kinematics of the two regions: the gas in the inner EELR could be affected by jet-induced shocks.

c) There is not clear evidence for anti-correlation between the widths of the lines and the ionization level of the original ion as due to the effects of shocks.

d) We find that the level of ionization of the inner EELR is noticeably lower than the level of ionization of the outer EELR and similar to that measured in other jet-cloud interaction targets. Interestingly the inner EELR shows also the broader lines.

Therefore, although PKS 1932-464 does not show compelling evidence for jet-cloud interactions, some of its characteristics suggest that, indeed, the radio jet is interacting with the ambient gas in the inner EELR. Obtaining spectra along the radio axis, where the strongest effects of the interaction are expected, will provide more definitive answers.

5.1. Alternative possibilities

Can we explain the properties of PKS 1932-464 in another way which does not involve the interaction between the radio jet and the ambient gas?

An expanding shell

The inner EELR corresponds, as we said before, to the feature in Fig. 1, which we named 'ARM'. This arm seems to have a faint extension which closes into a loop connected to the main body of the galaxy. Such morphology is reminiscent of an expanding shell which could be due, for instance to an outflowing wind. If the wind is sweeping material out, this could explain the morphology described in Sect. 3.1 , where a gap is seen between the arm and the main body of the galaxy.

An observable characteristic of outflowing winds is broadening of the lines (e.g. Legrand et al 1997) as is observed in the long wavelength component. Component B (the one more distant to the nucleus) could be more distant gas which has not yet been reached by the wind and therefore emits narrower lines. The different velocity shifts for the two components support this. The fact that the velocity shifts are smaller for component A (supposedly, the one expanding) could be explained if the direction of the expansion takes place close to the plane of the sky.

If the wind compresses the gas, the density enhancement would explain the low level of ionization observed for the gas in this region. We should explain, however, why component B shows also such low ionization level, if it has not been reached by the expanding shell.

Mergers or interactions between two galaxies

The projected thickness of the inner EELR (the 'ARM') is $\sim$12 kpc and length $\sim$30 kpc which could be a smaller galaxy which is cannibalized or being merged with PKS 1932-464. Interaction between galaxies can also disturb the kinematics of the ionized gas and the emission lines appear broad and/or with split components. Such is the case of the radio galaxy PKS0349-27 (Koekemoer & Bicknell 1994).

6. Summary and conclusions

Although PKS 1932-464 does not show compelling evidence for jet-cloud interactions, some of its characteristics suggest that such an interaction might be taking place.

We do not find the extreme properties observed in other jet-cloud interaction radio galaxies (striking correspondence between radio and optical structures, extreme motions, conclusive anti-correlation between line width and ionization level). However, this object presents two well differentiated EELR with very different kinematics and ionization level of the gas. The broader lines and split components in the inner EELR, its low ionization level and the fact that it lies well inside the radio structures could be explained in terms of shocks produced during the interactions between the radio structures and the emitting gas.

On the other hand, the narrow and single line profiles, the high ionization level of the gas and the fact that it lies outside the radio structures, suggest that the properties of the outer EELR are explained in terms of pure AGN illumination. It is also possible that this region is the precursor gas ahead of the shock and photoionized by its UV continuum.

PKS 1932-464 shares many similarities with high redshift radio galaxies: the radio lobe arm-ratio, radio depolarization and optical asymmetries. This suggests that, as in high redshift radio galaxies, the radio plasma is interacting strongly with the probably rich environment of PKS 1932-464.

We have considered two alternative scenarios to explain the observed properties of PKS 1932-464. One of them involves an outflowing wind which is forcing the gas in the inner EELR to expand, producing the broadening of the lines and the compression of the gas. It could also be that the inner EELR is a companion galaxy which is interacting with PKS 1932-464.

The spectroscopic information was obtained with a slit which was not exactly aligned along the radio axis. If the radio jet is interacting with the ambient gas we expect the strongest disturbances to take place near this direction. Obtaining long slit spectra along the radio axis can provide more conclusive answers.

The nuclear spectrum reveals the presence of a broad component in Hα which indicates that PKS 1932-464 is a broad line radio galaxy in which the AGN is observed directly. This explains the low level of polarization observed in the UV continuum of this object.

Acknowledgements. M.Villar-Martín thanks Jacco van Loon for useful discussions. M.Villar-Martín acknowledges support from PPARC grant. Thanks also to the referee for his/her useful comments.

References

Baum S.A., Heckman T., van Breugel W., 1990, ApJS, 74, 389
Best P.N., Longair M.S., Röttgering H.J.A., 1996, MNRAS, 280, L9
Binette L., Wang J.C.L., Zuo L., Magris C.M., 1993a, AJ, 105, 797
Binette L., Wang J.C.L., Villar-Martín M., Martin P.G., Magris C.M., 1993b, ApJ, 414, 535
Binette L., Wilson A.S., Storchi-Bergman T., 1996, A&A, 312, 365
Burstein D., Heiles C., 1984, ApJS, 54, 33-79
Cardelli J., Clayton G., Mathis J., 1989, ApJ, 345, 245
Carilli C.L., Perley R.A., Dreher. J.H., 1988, ApJ, 334, 73
Chambers K.C., Miley G.K., van Breugel W.J.M., 1987, Nature, 329, 604
Clark N.E. & Tadhunter C.N. 1996, in *Cygnus A– Study of a Radio Galaxy* (eds. Carilli C.L. & Harris D.E.), CUP, p15
Clark N.E., 1996, Phd Thesis, University of Sheffied
Clark N.E., Tadhunter C.N., Morganti R., Killeen N.B., Fosbury R.A.E., Hook R.N., Shaw M., 1997a, MNRAS, 286, 558
Clark N.E., Axon D., Tadhunter C.N., Robinson A., O'brien P., 1997b, ApJ, in press
Dickson R., 1997, Phd Thesis, University of Sheffied
Dopita M.A., Sutherland R.S., 1995, ApJ, 455, 468
Dopita M.A., Sutherland R.S., 1996, ApJS, 102, 161
Dreher J.W., Carilli C.L., Perley R.A., 1987, ApJ, 316, 611
Garrington S.T., Conway R.G., 1991, MNRAS, 250, 198
Greidanus H., Strom R.G., 1992, A&A, 257, 265
Heckman T.M., Illingworth G.D., Miley G.K., van Breugel W.J.M., 1985, ApJ, 299, 41
Jackson N., Sparks W.B., Miley G.K., Machetto F., 1993, A&A, 269, 128
Koekemoer A.M., Bicknell G.V., 1994, in Extragalactic Radio Sources, IAU 175, p. 473
de Koff S., Baum S., Sparks W., Biretta J., Golombek D., Macchetto F., McCarthy P., Miley G., 1996, ApJS, 1996, 107, 621
Legrand F., Kunth D., Mas-Hesse J.M., Lequeux J., 1997, A&A, in press
Liu R., Pooley G., 1991, MNRAS, 253, 669
McCarthy P.J., Spinrad H., Djorgovsky S., Strauss M.A., van Breugel W., Liebert J., 1987, ApJ, 319, L39
McCarthy P.J., van Breugel W., 1989, in *ESO Workshop on Extranuclear Activity in Galaxies* , eds. E. Meurs and R.A. Fosbury, ESO Conf. and Workshop Proc. no 32, p55
McCarthy P.J., Baum S., Spinrad H., 1996, ApJS, 106, 281
Morganti R., Oosterloo T.A., Reynolds J., Tadhunter C.N., Migenes V., 1997, MNRAS, 284, 541
Pedelty J.A., Rudnick L., McCarthy P.J., Spinrad H., 1989, AJ, 97, 647
Pentericci L., Roettgering H., Miley G., Carilli C., McCarthy P., 1997, A&A, 326, 580
Robinson A., Binette L., Fosbury R.A.E., Tadhunter C.N., 1987, MNRAS 227, 97
Röttgering H.J.A., West M., Miley G. & Chambers K. 1996, A&A, 307, 376
Siebert J., Brinkmann W., Morganti R., Tadhunter C.N., Danzinger I.J., Fosbury R.A.E., di Serego Alighieri S., 1996, MNRAS, 279, 1331
Tadhunter C.N., Fosbury R.A.E., Quinn P.J., 1989, MNRAS, 240, 225
Tadhunter C.N., 1990, in *New Windows to the Universe*, eds. F. Sánchez and M. Vázquez, Cambridge University Press, p175
Tadhunter C.N., Morganti R., di Serego Alighieri S., Fosbury R.A.E., Danzinger I.J., 1993, MNRAS, 263, 999
van Ojik R., Roettgering H., Carilli C.L., Miley G.K., Bremer M.N., Macchetto F., 1996, A&A, 313, 25

This article was processed by the author using Springer-Verlag LaTeX A&A style file *L-AA* version 3.